(Received 12 May 2025, Accepted 18 July 2025, Scheduled 1 August 2025)

Switched Reluctance Motor Based on Expanded State Observer Lehuy Model Predictive Current Control

Xiong Su[1], Aide Xu[2,*], and Shiling Lin[1]

[1] College of Electrical Engineering of Ships, Dalian Maritime University, Dalian 116026, China
[2] College of Information and Science Technology, Dalian Maritime University, Dalian 116026, China

ABSTRACT: Aiming at the issues of large current ripple and significant torque pulsation in switched reluctance motor (SRM) model predictive current control (MPCC) under varying operating conditions, this paper innovatively proposes a novel SRM model predictive current control method integrating an extended state observer (ESO) and Lehuy model. By constructing a nonlinear current prediction framework based on the Lehuy model, the data dependency on traditional Look-Up Table (LUT) methods is significantly reduced. Meanwhile, the real-time compensation of system disturbances is achieved by introducing the ESO, resolving parameter mismatch issues under dynamic operating conditions. Simulated and experimental results demonstrate that this method, implemented on a 12/8-pole SRM prototype, achieves a current ripple reduction of 41.5% and torque pulsation suppression of 32.7% compared to traditional LUT-MPCC. This research provides new insights into the robust control of SRMs in high-precision servo scenarios.

1. INTRODUCTION

Switched reluctance motor (SRM) has shown remarkable competitiveness in new energy fields such as new energy vehicles and industrial drives due to its advantages of simple structure, low manufacturing cost, and high fault-tolerance capability [1, 2]. However, the highly nonlinear characteristics of the magnetic circuit due to its biconvex pole structure are prone to magnetic saturation and local hysteresis effects, which in turn generate significant torque pulsations and electromagnetic noise. This problem not only exacerbates mechanical vibration and loss, but also leads to an increase in current ripple, which seriously restricts the application of SRMs in high-precision servo systems [3]. Therefore, how to effectively suppress the torque pulsation and current ripple has become one of the important research directions to improve the control performance of SRMs.

Aiming at the above problems, the existing researches mainly focus on the two major directions of structural optimization design and advanced control methods [4, 5]. In the field of advanced control methods, model predictive control (MPC) has received extensive attention in recent years due to its multi-objective optimization capability and strong adaptability to nonlinear systems [6]. Based on the difference of control objectives, MPC can be further classified into model predictive torque control (MPTC) and model predictive current control (MPCC): the former reduces pulsations by directly optimizing the torque trajectory [7], while the latter focuses on the improvement of current tracking accuracy to suppress ripples [8]. Ref. [9] proposes an MPTC method based on a linearized magnetic chain model, which is effective in reducing the storage requirement and computation time, but its reliance on the Look-Up Table (LUT) model still leads to insufficient suppression of high-frequency torque fluctuations. Ref. [10] adopts the Lehuy analytical model to replace the LUT model, and optimizes the voltage vector selection by combining with the sector adaptive allocation technique, which improves the torque-current ratio while reducing the computational complexity, but the parameter mismatch problem under the dynamic working condition has not been solved. Ref. [11] introduces a finite-time domain linear quadratic regulator (LQR) with Kalman filter to enhance the model robustness through online calibration of inductor parameters; however, the introduction of adaptive algorithms significantly increases the system complexity. Ref. [12] proposes a model-free predictive current control method based on a hyperlocal model, which avoids the dependence on an accurate mathematical model, but its observer design is sensitive to the current derivative noise, and the computational cost is high.

The performance of model prediction is affected by model parameter mismatches and various disturbances. For this reason, scholars have integrated observer technologies into the predictive framework to achieve disturbance compensation [13]. Existing disturbance compensation observers for SRMs have obvious limitations: adaptive observers rely on accurate models, show poor adaptability to the strong nonlinearity of SRMs, and their parameter adaptive laws increase the computational load by more than 30% compared with the basic MPCC [14]; sliding mode observers depend on the precise design of sliding mode gains, and the fixed gain makes it difficult to balance chattering and dynamic response. Moreover, in multi-phase SRMs, the observation accuracy decreases by 15%–20% due to inter-phase coupling [15].

* Corresponding author: Aide Xu (aidexu@dlmu.edu.cn).

The linear extended state observer (LESO) is adopted in this paper, which has significant advantages: it does not require an accurate model of the object, regards parameter perturbations, external disturbances, and unmodeled dynamics as a lumped disturbance for estimation, and avoids the chattering of sliding mode observers and the model dependence of adaptive observers in principle; its linear structure results in a computational complexity that is only 60% of that of sliding mode disturbance observer (SMDO) [16], making it more suitable for real-time control; its dynamic adjustment mechanism enhances noise robustness, whereas SMDO and similar observers tend to amplify noise due to high-frequency switching, requiring additional filtering which leads to a phase lag increase of more than 5°.

It should be noted that recent studies have explored deep learning-based model predictive control methods [17], which show potential in nonlinear disturbance compensation through end-to-end learning mechanisms that directly map inputs to control outputs. However, such methods usually require massive training data and high computing power, making them difficult to meet the requirements of industrial scenarios for real-time performance and limited computing resources. Thus, this paper still focuses on the fusion strategy of observers and analytical models.

In this paper, we propose a Lehuy model predictive current control method for switched reluctance motor (SRM) based on extended state observer (ESO), aiming at solving the problems of large data dependence of the traditional LUT model, inaccuracy of the Lehuy model, and insufficient compensation of the unknown perturbations. Specifically, 1) analyze the principle of LUT model predictive current control, based on which the Lehuy model is introduced to reduce the model dependence of SRM predictive current, 2) design the expanded state observer for real-time observation of aggregate disturbances and introduce them into the framework of Lehuy model predictive current control, so as to further reduce torque pulsations and current ripples. The simulated and experimental results show that the torque pulsation and phase current ripple can be effectively suppressed, which provides a new idea for the high-performance control of SRM.

2. CONVENTIONAL SRM MODEL PREDICTIVE CURRENT CONTROL

2.1. Power Converters

In this paper, a three-phase 12/8-pole SRM is used as the driving body, and its supporting power converter adopts the asymmetric half-bridge topology shown in Fig. 1.

When the SRM operates normally, the operation modes of the bridge arms of each phase of the power converter mainly include positive voltage excitation, zero-voltage continuity, and negative voltage demagnetization. As shown in Fig. 1, U_{dc} is the DC bus voltage; s_1 and s_2 are the power triodes; and D_1 and D_2 are the continuity diodes. When the power transistors s_1 and s_2 are conducting, the motor winding is in the excitation mode. At this time, the DC power supply provides positive voltage excitation current to the winding through s_1 and

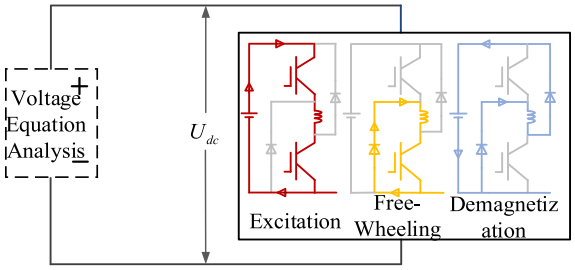

FIGURE 1. 12/8-pole switched reluctance motor power converter.

s_2. In this mode, the winding current increases gradually to provide the motor with the required torque; when the power transistor s_1 is off and s_2 on, the winding terminal voltage is zero, and it is in the zero-voltage continuity mode. At this time, the winding current continues through the continuity diodes D_1 and D_2. In this mode, the winding current remains unchanged, and the motor continues to output torque; when the power transistors s_1 and s_2 are off, the winding current gradually drops to zero and enters the negative voltage demagnetization mode. At this time, the winding current forms a closed loop through the continuity diodes D_1 and D_2. In this mode, the winding current decreases rapidly, and the demagnetization process is completed. The output signal of switching vector selection can be expressed as Eq. (1) in this operating state:

$$S_p\,|_{p=1,2,3} = \begin{cases} -1, & \text{Demagnetization} \\ 0, & \text{Free-Wheeling} \\ 1, & \text{Magnetization} \end{cases} \tag{1}$$

2.2. Conventional Model Predictive Current Control

The SRM voltage equation is:

$$U(t) = Ri(t) + \frac{\partial\psi(t)}{\partial i}\frac{di(t)}{dt} + \frac{\partial\psi(t)}{\partial\theta}\frac{d\theta(t)}{dt} \tag{2}$$

where U is the phase voltage, R is the phase resistance, i the phase current, ψ the magnetic chain value, and θ the rotor position.

Considering the three-phase structural characteristics of the SRM, single-phase is usually modeled to simplify the analysis process. By performing a single-phase analysis of Eq. (2) and combining it with the discretization process, the following discretization equations can be derived

$$\begin{cases} \psi_p(k+1) = \psi_p(k) + (U_p(k) - i_p(k)R_p)\Delta t \\ \theta_p(k+1) = \theta_p(k) + \omega(k)\Delta t \end{cases} \tag{3}$$

where $\psi_p(k)$, $U_p(k)$, $i_p(k)$, $\theta_p(k)$, $\omega(k)$ denote the phase magnetic chain, phase voltage, phase current, phase angle, and angular velocity at the kth moment, and $\psi_p(k+1)$, $\theta_p(k+1)$ denote the phase magnetic chain and phase angle at the $k+1$st moment, respectively.

The principle of LUT model prediction is shown in Fig. 2. Firstly, the next moment of $\psi_p(k+1)$ is found by discretizing the magnetic chain equation; secondly, based on the current

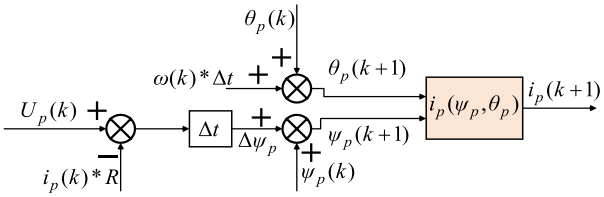

FIGURE 2. Schematic diagram of LUT model prediction.

moment rotational speed of $\omega(k)$, the next moment of $\theta_p(k+1)$ is found by the equation of mechanical motion; and finally, combining with the predicted $\psi_p(k+1)$ and $\theta_p(k+1)$, the predicted value of the next moment of the phase current of $i_p(k+1)$ is found by the LUT. Because SRM has serious nonlinear characteristics, its current changes with the magnetic chain and rotor position, and in order to predict the next current, it is necessary to establish a LUT to store the data of the three. The data in Fig. 3 are obtained by inverse interpolation of $\psi(i,\theta)$.

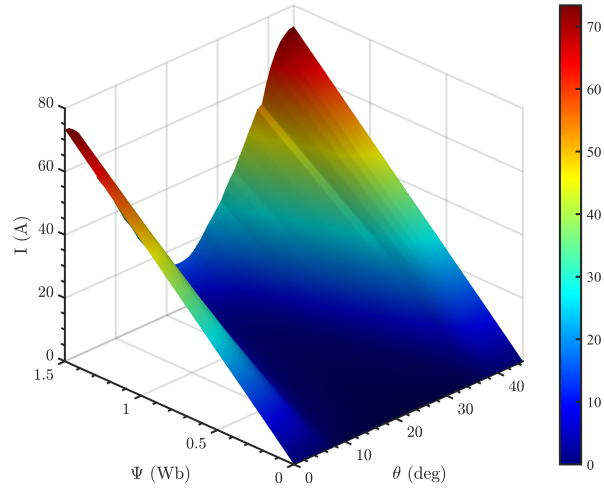

FIGURE 3. Phase current linkage of SRM versus phase flux linkage and rotor position.

As can be seen from Fig. 4, in this paper the cost function only considers the current term and does not include other terms such as the magnetic chain, so there is no need to adjust the weight system. The cost function is defined as:

$$J = |i_{ref}(k+1) - i(k+1)| \tag{4}$$

Figure 4 shows the block diagram of predictive current control for SRM conventional model, which demonstrates the dual closed-loop control method of speed and current by combining

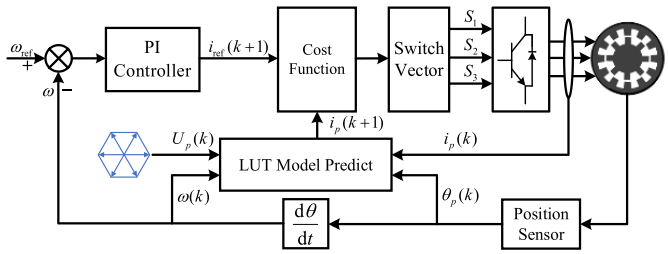

FIGURE 4. Block diagram of SRM conventional model predictive current control.

the predictive current control with the speed closed-loop control. The outer speed loop is responsible for tracking the reference speed and the inner current loop responsible for tracking the reference current. The method utilizes a proportional-integral (PI) controller to calculate the reference current $i_{ref}(k+1)$ and at the same time predicts the phase current $i_p(k+1)$ at the next moment by real-time measurement of rotor position $\theta_p(k)$, phase current $i_p(k)$, and phase voltage $U_p(k)$ as shown in Fig. 2. The predicted current value $i_p(k+1)$ is compared with the reference current $i_{ref}(k+1)$ in the evaluation function module to generate evaluation indexes to guide the selection of switching vectors, so as to realize accurate control of motor current and ensure the closed-loop control performance of the system.

The LUT construction of the traditional MPCC method relies on blocking experiments, which is a time-consuming process and requires a lot of data processing [8], so there is a need to develop a simple and fast analytical modeling method to efficiently obtain torque and magnetic chain data.

3. LEHUY MODEL PREDICTIVE CURRENT CONTROL OF SWITCHED RELUCTANCE MOTORS BASED ON EXPANDED STATE OBSERVER

3.1. Lehuy Modeling

As shown in Fig. 5, the Lehuy model is able to effectively capture the nonlinear relationship among magnetic chains, currents, and angles by utilizing the chain-current relationship at the centered and uncentered positions. This model not only reduces the data requirements, but also improves the modeling accuracy [15].

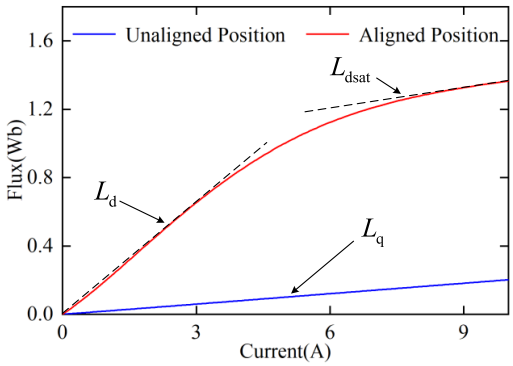

FIGURE 5. Chain-current characteristic curves at centered and uncentered positions.

The expression for $\psi_p(i_p,\theta_p)$ based on the Lehuy model is:

$$\psi_p(i_p,\theta_p) = L_q i_p + \left[L_{\text{dsat}} i_p + A(1-e^{-Bi}) - L_q i_p\right] \times f(\theta_p) \tag{5}$$

where $f(\theta)$, A, B can be expressed as respectively:

$$\begin{cases} f(\theta_p) = \left(2N_r^3/\pi^3\right)\theta_p^3 - \left(3N_r^2/\pi^2\right)\theta_p^2 + 1 \\ A = \psi_m - L_{\text{dsat}} I_m \\ B = \left(L_d - L_{\text{dsat}}\right)/\left(\psi_m - L_{\text{dsat}} I_m\right) \end{cases} \tag{6}$$

where N_r is the number of rotor pole pairs; L_q and L_d are the inductance values at the non-aligned and aligned positions of

the stator and rotor pole centers, respectively; L_{dsat} is the saturation inductance value at the aligned position; and ψ_m and I_m are the maximum values of the magnetic chain and inductance, respectively.

From the two flux curves in Fig. 5, all the parameters of the Lehuy model can be obtained, and then the full-period flux curves are calculated according to Eq. (5).

As can be seen in Fig. 6, the Lehuy model basically overlaps with the magnetic chain model observed by the plug-and-rotate experimental method, and the observation accuracy is high.

$$i_p(k) = \int_0^t \frac{\partial i_p(k)}{\partial \psi_p(k)} \left[U_p(k) - i_p(k)R - \left[\frac{\partial \psi_p(k)}{\partial \theta_p(k)} \right] \omega(k) \right] dt \tag{7}$$

where $\partial\psi_p(k)/\partial\theta_p(k)$ and $\partial\psi_p(k)/\partial i_p(k)$ can be derived from Eq. (5):

$$\begin{cases} \partial\psi_p/\partial\theta_p = \left[L_{\text{dsat}} i_p(k) + A\left(1 - e^{-Bi_p(k)}\right) - L_q i_p(k) \right] \\ \qquad\qquad f'[\theta_p(k)] \\ \partial\psi_p/i_p = L_q + \left[L_{\text{dsat}} + ABe^{-Bi_p(k)} - L_q \right] f\left[\theta_p(k)\right] \end{cases} \tag{8}$$

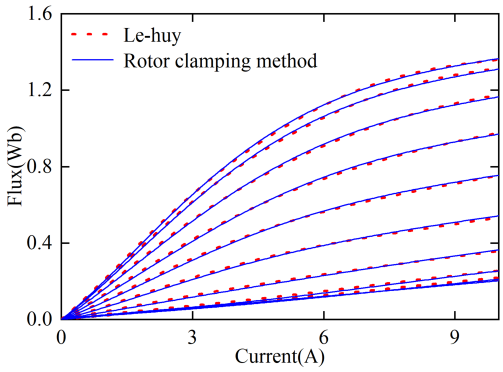

FIGURE 6. Comparison of the Lehuy model and the plug-and-rotate experimental method for magnetic chain prediction.

Associatively Eq. (5), Eq. (7), and Eq. (8), the next predicted current value $i_p(k+1)$ can be derived:

$$i_p(k+1) = i_p(k) + \frac{\partial i_p(k)}{\partial \psi_p(k)} \left[U_p(k) - i_p(k)R - \left[\frac{\partial \psi_p(k)}{\partial \theta_p(k)} \right] \omega(k) \right] \Delta t \tag{9}$$

According to Eq. (9), the Lehuy model predicts the current principle as shown in Fig. 7. Compared with the LUT method, the Lehuy modeling method is simpler and faster; the SRM modeling requires only five parameters; the analytical model is more suitable for the controller design of MPC, and it is also compatible with various complex algorithms.

3.2. Expansion State Observer Design

In order to further improve the Lehuy model prediction current accuracy, ESO is introduced in this section for perturbation

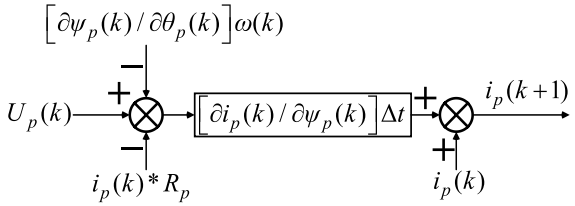

FIGURE 7. Lehuy model prediction current schematic diagram.

compensation. The real-time estimation and compensation of the prediction error of the whole model by ESO can effectively improve the accuracy of the model prediction, thus enhancing the overall performance of the control system.

Considering the parameter variations and unknown perturbation terms, the voltage equation (2) can be changed to:

$$\begin{aligned} U(k+1) &= (R+\Delta R)i + \left(\frac{\partial \psi}{\partial i} + \Delta \frac{\partial \psi}{\partial i} \right) \frac{di}{dt} \\ &+ \left(\frac{\partial \psi}{\partial \theta} + \Delta \frac{\partial \psi}{\partial \theta} \right) \frac{d\theta}{dt} + f(k) \end{aligned} \tag{10}$$

where ΔR is the value of resistance change, $\Delta(\partial\psi/\partial i)$ the amount of change in the bias conductance of the magnetic chain to the current, $\Delta(\partial\psi/\partial\theta)$ the amount of change in the bias conductance of the magnetic chain to the angle, and $f(k)$ the amount of unknown disturbance, defining the above set of total disturbances as $F(k)$.

In order to introduce the total perturbation $F(k)$ into LESO and reduce the LESO observation burden, the total perturbation $F(k)$ needs to be further analyzed.

Considering the nonlinear characteristics of switched reluctance motors and the complexity of the operating environment, the total perturbation $F(k)$ can be divided into three parts: parametric ingress, external load perturbation, and unmodeled dynamics.

Considering the time-varying characteristics (e.g., temperature drift, magnetic saturation effects) of the inductor L and resistor R, the parameter uptake perturbation can be subdivided into.

$$\begin{cases} \Delta R = \alpha_R \cdot i_p(t) \\ \Delta L = \alpha_L \cdot \tanh\left(\frac{i_p(t)}{I_{\text{dsat}}} \right) \end{cases} \tag{11}$$

where α_R and α_L are the inductance coefficients, and I_{dsat} is the inductance saturation threshold.

Considering sudden mechanical load changes or frictional torque fluctuations, external load disturbances can be subdivided into:

$$\tau_{\text{load}}(t) = \beta_0 + \beta_1 \sin(\omega_{\text{load}} t) \tag{12}$$

where β_0 and β_1 are load intensity parameters, and ω_{load} is the disturbance frequency.

Considering the high-frequency switching noise with magnetic chain harmonic components, the unmodeled dynamic perturbation can be subdivided into:

$$f_{\text{high}}(t) = \sum_{k=1}^{N} c_k e^{-\lambda_k t} \sin(\omega_k t) \tag{13}$$

where c_k, λ_k, and ω_k are high frequency noise parameters.

Integrating the above perturbation analysis into Eq. (10) yields the extended state space model:

$$\begin{cases} \dot{x}_1 = x_2 \\ \dot{x}_2 = -\frac{R}{L(x)}x_1 + \frac{1}{L(x)}U - \frac{1}{L(x)}\tau_{\text{total}} + \delta \\ y = x_1 \end{cases} \tag{14}$$

where τ_{total} is the sum of the external load perturbation τ_{load} and unmodeled dynamic perturbation f_{high}; the inductance time-varying term $\delta = \frac{\partial L}{\partial i_p}\dot{i}_p + \frac{\partial L}{\partial \theta_p}\dot{\theta}_p$ and matches the nonlinear function $L(x)$ of the inductance L with respect to the current i_p. Considering only the current can be simplified to $L(x) = L(i_p) = L_q + (L_d - L_q) \cdot f(i_p)$.

$$\begin{cases} \dot{\hat{x}}_1 = \dot{\hat{x}}_2 + g_1(y - \hat{x}_1) \\ \dot{\hat{x}}_2 = -\frac{R}{L(\hat{x}_1)}\hat{x}_1 + \frac{1}{L(\hat{x}_1)}U + g_2(y - \hat{x}_1) + \hat{F} \\ \hat{F} = \omega_0^2(y - \hat{x}_1) - 2\varsigma\omega_0\hat{x}_2 \end{cases} \tag{15}$$

where $\hat{F}$ is the estimated value of the total perturbation $F(k)$; $\hat{x}_1$, $\hat{x}_2$ are the current value and current derivative value estimated by LESO, respectively; ς is the damping coefficient, which is usually taken as the critical damping value 0.707; and ω_0 is the observer bandwidth.

The values of g_1 and g_2 can be calculated from ω_0 and ς:

$$\begin{cases} g_1 = 2\varsigma\omega_0 L_0 \\ g_2 = \omega_0^2 L_0 \end{cases}$$

where L_0 is the nominal inductance value, and 50 mH can be taken here.

3.3. Stability Analysis

Let the error equation of LESO be:

$$\begin{cases} \dot{e}_1 = e_2 \\ \dot{e}_2 = -\frac{R}{L(x)}e_1 + \frac{1}{L(x)}\left(U - \hat{U}\right) - \frac{1}{L(x)}\tilde{\tau} + \delta \end{cases} \tag{16}$$

where e_1, e_2 are the difference between the estimated and actual values of current and current derivative of LESO, respectively, and $\tilde{\tau}$ is the total disturbance estimation error.

The dynamic deviation between the total disturbance $F(k)$ and its estimated value $\hat{F}(k)$ by the LESO is defined as the disturbance estimation error η. Since I_{dsat} and α_R are known constants in engineering applications, the amplitudes of ΔR and ΔL are bounded. Meanwhile, β_0 and ω_{load} are determined by operating conditions, and it can be assumed that they satisfy $|\beta_0| \leq \beta_{\max}$ and $\omega_{\text{load}} \leq \omega_{\max}$. In addition, the amplitude of unmodeled dynamics is limited by the switching frequency of power devices and the cutoff frequency of filters. Therefore, the amplitude of the total disturbance $F(k)$ satisfies $|F(k)| \leq F_{\max}$, and further, the amplitude of η can be designed to satisfy $|\eta| \leq \eta_{\max}$ by adjusting the bandwidth ω_0 of the LESO.

If the inductance parameter changes slowly, one can linearize $L(x)$ at the nominal value L_0 [18]:

$$\frac{1}{L(x)} \approx \frac{1}{L_0} - \frac{\Delta L}{L_0^2}i_p \tag{17}$$

Under the condition of a sufficiently large observer bandwidth, substituting into the error equation and neglecting higher-order terms leads to the linearized error model:

$$\begin{bmatrix} \dot{e}_1 \\ \dot{e}_2 \end{bmatrix} = \begin{bmatrix} 0 & 1 \\ -\frac{R}{L_0} & 0 \end{bmatrix}\begin{bmatrix} e_1 \\ e_2 \end{bmatrix} + \begin{bmatrix} 0 \\ \frac{1}{L_0} \end{bmatrix}\left(U - \hat{U}\right) + \begin{bmatrix} 0 \\ -\frac{1}{L_0} \end{bmatrix}\tilde{\tau} \tag{18}$$

The pole configuration method allows the observer gain to be determined as $G = \begin{bmatrix} g_1 & g_2 \end{bmatrix}^T$, such that the characteristic root of the error dynamic matrix lies in the left half of the complex plane. Define the standard form of the error dynamic equation:

$$\dot{e} = A_e e + B_e\left(U - \hat{U}\right) + B_e\tilde{\tau} \tag{19}$$

Among them:

$$A_e = \begin{bmatrix} 0 & 1 \\ -\frac{R}{L_0} & 0 \end{bmatrix}, \quad B_e = \begin{bmatrix} 0 \\ \frac{1}{L_0} \end{bmatrix}$$

Select the observer gain:

$$G = \begin{bmatrix} g_1 \\ g_2 \end{bmatrix} = \begin{bmatrix} 2\varsigma\omega_0 L_0 \\ \omega_0^2 L_0 \end{bmatrix} \tag{20}$$

such that the characteristic equation of the error dynamic matrix $A_e - B_e G$ is:

$$s^2 + 2\varsigma\omega_0 s + \omega_0^2 = 0 \tag{21}$$

Constructing Lyapunov functions:

$$V(e) = \frac{1}{2}e^T e \tag{22}$$

Derivation of Eq. (22) yields:

$$\dot{V} = e^T\dot{e} = e^T\left(A_e e + B_e\left(U - \hat{U}\right) + B_e\tilde{\tau}\right) \tag{23}$$

Proceed to the next step of derivation":

$$\dot{V} = e^T A_e e + \frac{1}{L_0}e_2\left(U - \hat{U}\right) - \frac{1}{L_0}e_2\tilde{\tau} \tag{24}$$

As the observer design is satisfied:

$$U - \hat{U} = G^T e \tag{25}$$

Further derivation can be made based on Equation (25):

$$\dot{V} = e^T\left(A_e e + \frac{G^T}{L_0}e_2\right) - \frac{e_2}{L_0}\tilde{\tau} \tag{26}$$

This is then combined with the above equation and organized to give:

$$\dot{V} = -e_1^2 - \varsigma\omega_0 e_2^2 + \frac{e_2}{L_0}\tilde{\tau} - \frac{e_2}{L_0}\hat{\tau} \tag{27}$$

If the perturbation estimation error is bounded, i.e., $|\tilde{\tau}| \leq \eta$, then:

$$\dot{V} \leq -e_1^2 - \varsigma\omega_0 e_2^2 + \frac{\eta}{L_0}|e_2| \tag{28}$$

By choosing a sufficiently large observer bandwidth ω_0, the second term can be made dominant and thus guaranteed:

$$\dot{V} < 0,\ \forall e_{1,2} \neq 0 \tag{29}$$

The error system is globally asymptotically stable according to the Lyapunov stability theorem.

3.4. Proposed Algorithm

The estimate of LESO for the total disturbance is obtained by substituting it into Eq. (9):

$$i_p(k+2) = \frac{\partial\hat{i}_p(k+1)}{\partial\psi_p(k)}\left[U_p(k) - \hat{i}_p(k+1)R - \left[\frac{\partial\psi_p(k)}{\partial\theta_p(k)}\right]\omega(k)\right]\Delta t + \hat{i}_p(k+1) - \hat{F}(k) \tag{30}$$

Based on the established Lehuy model, expanded state observer and predicted values, the following Expanded State Observer Based Predictive Current Control for Switched Reluctance Motor Lehuy Model method is obtained. As shown in Fig. 8, the reference current at the next moment is obtained based on the Lehuy model. The system perturbation is obtained from the established LESO, and the switching vector selection is realized based on the set turn-on angle, turn-off angle, evaluation function, and rotor position angle. The overall control strategy is a speed-current double closed-loop control scheme, where the inner loop is realized based on the predicted reference current and phase winding currents and is responsible for current tracking control. The outer loop is realized based on the motor rotor position information obtained from the encoder and is responsible for the reference speed tracking, and the closed-loop controller is a proportional-integral controller. The robustness of the adopted method is enhanced by real-time observation when resistance or voltage variations are introduced. The flowchart of the proposed implementation of the Lehuy model predictive current control of switched reluctance motor based on the expanded state observer is shown in Fig. 9. The predictive control set of the windings of each phase in the on-state interval contains $S_p = 1$ and $S_p = 0$, and the operating mode of the windings of each phase in the off-state interval is selected as $S_p = -1$.

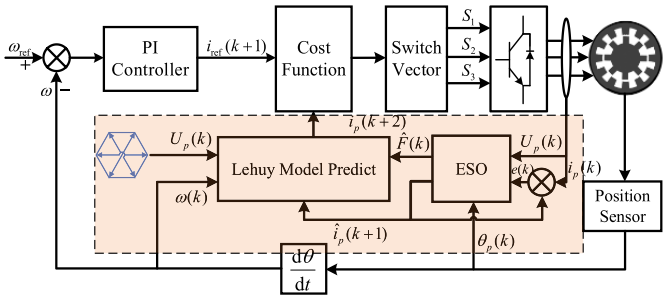

FIGURE 8. Control block diagram of the proposed algorithm.

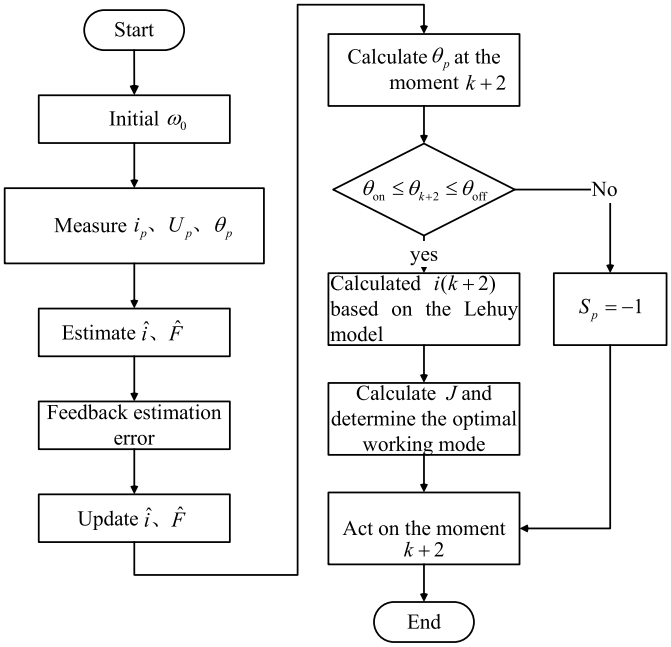

FIGURE 9. Flowchart of the proposed algorithm.

4. SIMULATION AND EXPERIMENTAL ANALYSIS

4.1. Simulation Analysis

A simulation model of a three-phase switched reluctance motor is established for verifying the feasibility and effectiveness of the proposed method. The simulation model mainly includes modules such as the electromechanical equation module, asymmetric half-bridge power converter module, control signal generation module, and motor winding module. For the control methods, the LUT model predictive control method, Lehuy model predictive control method, and the proposed algorithm are selected respectively, with the key parameters given in Table 1.

TABLE 1. Parameters of SRM prototype.

Parameter name	Parameter value
Number of stator and rotor pole pairs/(P_n)	12/8
Rated voltage/(V)	540
Rated torque/(N-m)	35
Rated speed/(r/min)	1500
Stator resistance/(Ω)	1.472
Power/(kW)	5.5
Rated current/(A)	11.3

The low-speed condition: load torque is 10 N-m, and the given speed is 800 r/min.

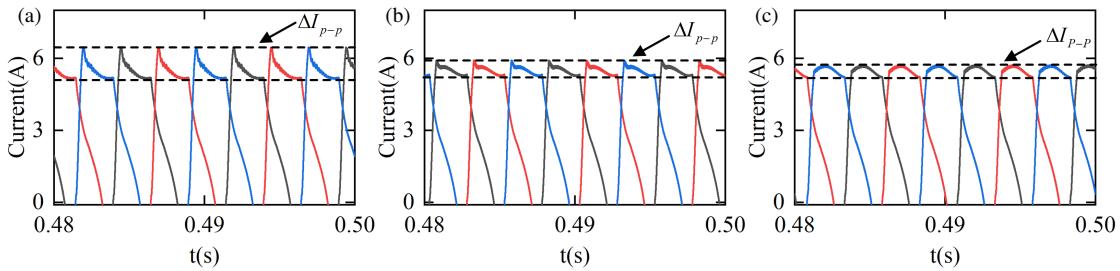

FIGURE 10. Comparison results of current waveform simulation under low-speed working condition. (a) LUT-MPCC method in [8]. (b) Lehuy-MPCC method in [15]. (c) Proposed algorithm.

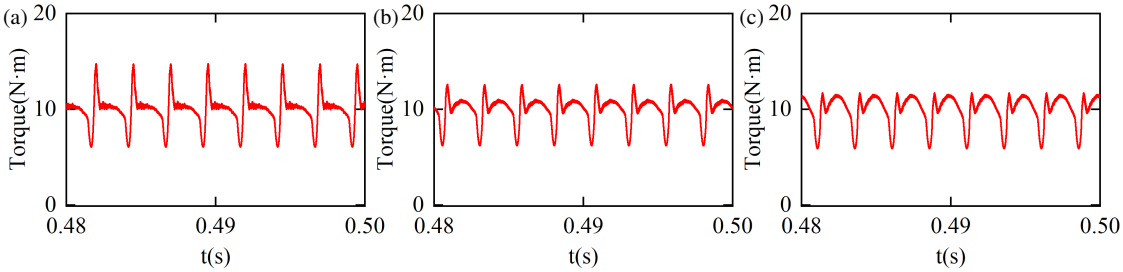

FIGURE 11. Comparison results of torque waveform simulation under low speed and heavy load conditions. (a) LUT-MPCC method in [8]. (b) Lehuy-MPCC method in [15]. (c) Proposed algorithm.

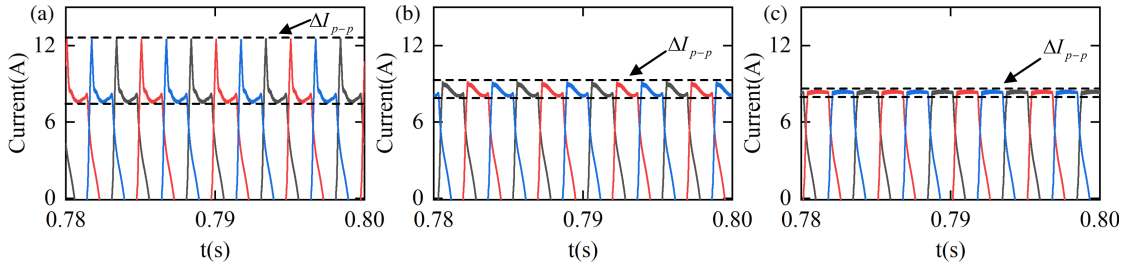

FIGURE 12. Comparison results of current waveform simulation under high-speed working condition. (a) LUT-MPCC method in [8]. (b) Lehuy-MPCC method in [15]. (c) Proposed algorithm.

Figure 10 compares the phase current ripple characteristics of the three MPCC methods under low-speed operating conditions: the peak current ripple of LUT-MPCC is 1.26 A; Lehuy-MPCC reduces it to 0.73 A, and the Lehuy-ESO-MPCC proposed in this paper further reduces it to 0.52 A. Compared with LUT-MPCC and Lehuy-MPCC, the Lehuy-ESO-MPCC reduces the current ripple by 58.7% and 28.8%, respectively, indicating that the disturbance compensation mechanism of ESO effectively reduces the current fluctuation.

Figure 11 compares the torque pulsation characteristics of the three MPCC methods at low-speed operating conditions: the peak torque pulsation of LUT-MPCC is 86.91% of the rated torque; Lehuy-MPCC reduces it to 63.95%; and the Lehuy-ESO-MPCC proposed in this paper further reduces it to 52.04%. Compared with LUT-MPCC and Lehuy-MPCC, the torque pulsation amplitude of Lehuy-ESO-MPCC is reduced by 40.1% and 18.6%, respectively. The results show that the dynamic compensation of nonlinear magnetic chain perturbation by ESO effectively suppresses the interphase torque coupling effect and significantly improves the torque output smoothness.

The high speed condition: load torque is 20 N-m, and the given speed is 1500 r/min.

Figure 12 compares the phase current ripple characteristics of the three MPCC methods under high-speed operation: the peak current ripple of LUT-MPCC is 4.87 A; Lehuy-MPCC reduces it to 3.06 A; and the Lehuy-ESO-MPCC proposed in this paper further reduces it to 1.36 A. Compared with LUT-MPCC and Lehuy-MPCC, the Lehuy-ESO-MPCC reduces the current ripple by 63.8% and 55.6%, respectively. The results show that ESO can still effectively compensate time-varying characteristics of the inductor parameters and phase change disturbances under high-speed operation, which significantly improves the current tracking performance.

Figure 13 demonstrates the torque pulsation suppression effect of the three MPCC methods under high speed and heavy load conditions. For LUT-MPCC method, the accumulation of the magnetic chain interpolation error results in a peak torque pulsation of 114.7% of the rated torque. In contrast, Lehuy-MPCC method reduces the torque pulsation to 81.53% by simplifying the magnetic chain calculation, but the method still suf-

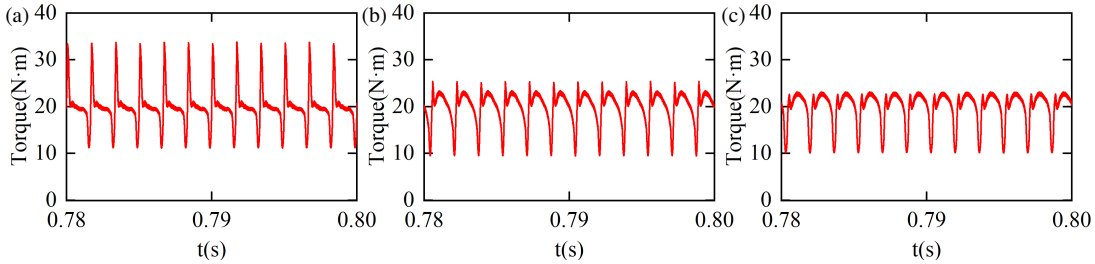

FIGURE 13. Comparison results of current waveform simulation under high-speed working condition. (a) LUT-MPCC method in [8]. (b) Lehuy-MPCC method in [15]. (c) Proposed algorithm.

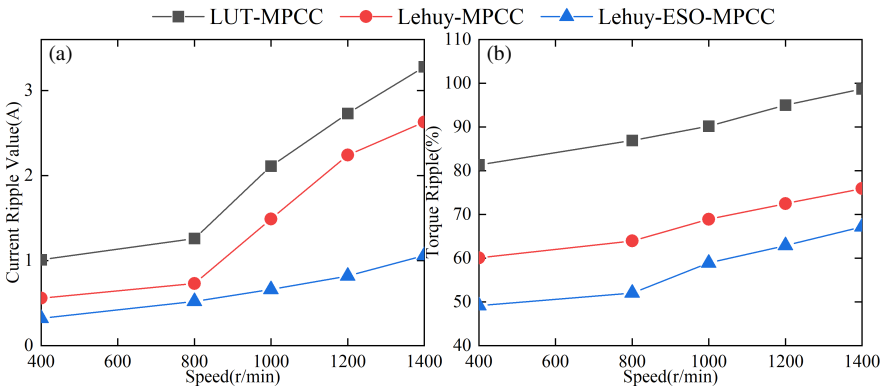

FIGURE 14. Comparison of simulation performance. (a) Current ripple. (b) Torque ripple.

fers from unmodeled cross-saturation effect. The Lehuy-ESO-MPCC method proposed in this paper further suppresses the torque pulsation to 70.48% by utilizing ESO for online compensation. Compared with LUT-MPCC and Lehuy-MPCC, the proposed method achieves 38.6% and 13.5% reduction in torque pulsation suppression, which validates the advantages of ESO in dealing with complex nonlinear coupling scenarios.

Based on the data analysis in Fig. 14(a), the Lehuy-ESO-MPCC method significantly reduces the current ripple from 1.0 A to 0.52 A compared to the LUT-MPCC and Lehuy-MPCC methods over the speed range of 400 r/min to 1400 r/min, exhibiting 58.7% and 28.8% reduction rates. In addition, Fig. 14(b) shows that the Lehuy-ESO-MPCC method also performs the best in suppressing torque pulsation in the same speed range, reducing the torque pulsation from 80% to 60%, realizing a reduction of 20% and 18.6%. These results show that the Lehuy-ESO-MPCC method is effective in suppressing current ripple and torque pulsation over the full speed range, further validating the effectiveness of its control method.

In the low-speed operation condition of switched reluctance motors, due to low rotor speed, the rotational electromotive force generated in the windings is small, resulting in a high rate of change of phase currents. This characteristic enhances the current tracking performance so that the output torque can follow the given value better, but at the same time, it also creates the problem of excessive phase current peaks. As the rotational speed is increased to the high-speed region, the rotational electromotive force increases significantly leading to a decrease in the rate of change of the current, at which time the phase current cannot effectively track the reference value, triggering a decrease in the torque tracking capability, accompanied by significant torque pulsation and current ripple problems [19]. After the introduction of the expanded state observer for phase current observation, its observation compensation mechanism can effectively reduce the deviation of the actual phase current from the reference value at high speed, which makes the proposed control algorithm show better current ripple suppression effect at high speed operation.

4.2. Experimental Analysis

The experimental platform is mainly composed of SRM control circuit, dSPACE console, crushing brake, torque sensor, and a 12/8 SRM, as specifically shown in Fig. 15.

In Fig. 16, the experimental results for low-speed operating conditions show that the Lehuy-ESO-MPCC algorithm achieves significant improvements in both current ripple and torque pulsation suppression. Compared with the peak current ripple of 1.32 A in the traditional LUT-MPCC method, the proposed algorithm reduces the ripple amplitude to 0.57 A by LESO compensation, which is 56.8%, and further reduces it by 29.6% compared with 0.81 A in the Lehuy-MPCC. At the level of torque pulsation suppression, the proposed method successfully compresses the pulsation amplitude from 85.7% in LUT-MPCC and 71.3% in Lehuy-MPCC to 58.3%, realizing relative reductions of 31.9% and 18.2%, respectively. The deviation of the experimental data from the simulation prediction is less than 3.5%, which verifies the robustness of the method to magnetic saturation nonlinearity and parameter uptake, and is in general agreement with the simulation results.

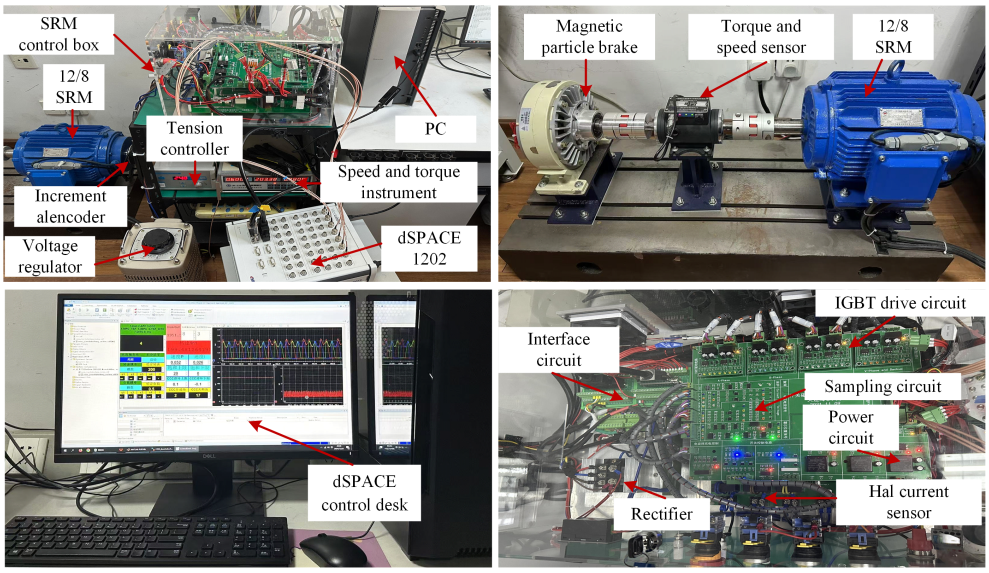

FIGURE 15. SRM experimental platform.

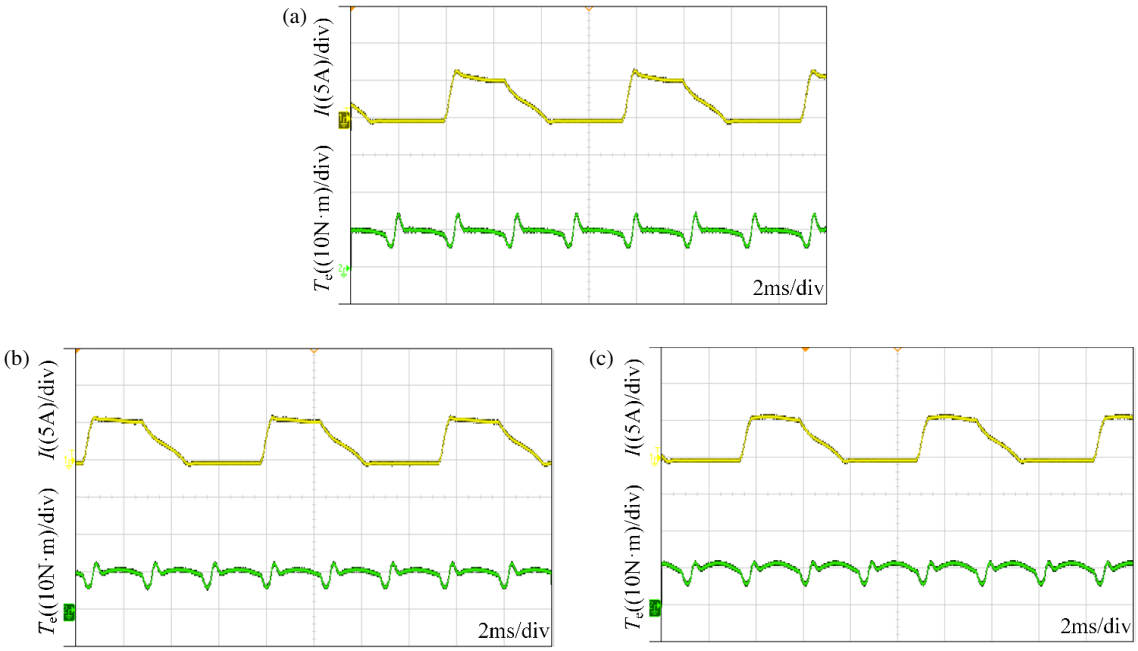

FIGURE 16. Experimental comparison results of current and torque waveforms under low-speed operating conditions. (a) LUT-MPCC method in [8]. (b) Lehuy-MPCC method in [15]. (c) Proposed algorithm.

In Fig. 17, the experimental results of high-speed working conditions show that the proposed Lehuy-ESO-MPCC algorithm exhibits significant advantages in current and torque control performance. Compared with the peak current ripple of 5.12 A in the LUT-MPCC method, the proposed algorithm suppresses the ripple amplitude to 1.42 A through real-time compensation of LESO, which is a reduction of 72.3%, and the phase offset is controlled within 0.5°; the ripple is further reduced by 61.4% compared with the 3.68 A in the Lehuy-MPCC method, which verifies the ability to accurately track the transient characteristics of the chain under high-speed operating conditions. In terms of torque pulsation suppression, the proposed method reduces the pulsation amplitude from 113.5% in the LUT-MPCC and 84.6% in the Lehuy-MPCC to 71.9%, which is 36.7% and 15.1%, respectively, and the trend is consistent with the simulation prediction. The experimental data show that the designed compensation mechanism is still effective in suppressing perturbations such as parameter uptake in the high-speed domain, verifying the strong robustness of the algorithm.

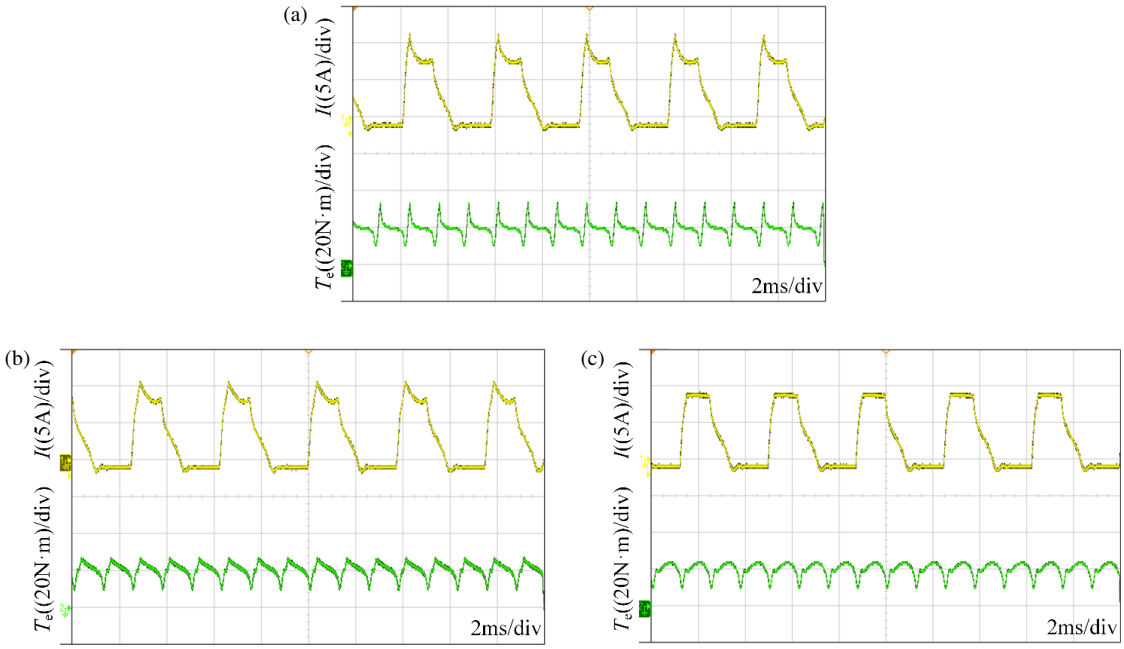

FIGURE 17. Experimental comparison results of current and torque waveforms under high-speed operating conditions. (a) LUT-MPCC method in [8]. (b) Lehuy-MPCC method in [15]. (c) Proposed algorithm.

5. CONCLUSION

In this paper, a Lehuy model predictive current control method for switched reluctance motors based on an expanded state observer is proposed to solve the current ripple and torque pulsation problems in the MPCC of SRMs. By constructing the predictive current equation using Lehuy model and designing ESO to compensate the total perturbation, the proposed method effectively suppresses the current ripple and torque pulsation while maintaining a low computational complexity. Specifically, the method reduces the torque pulsation by about 32.7% and the phase current ripple by about 41.5%, providing a new approach for high-performance control of SRMs.

REFERENCES

[1] Sun, X., N. Wang, M. Yao, and G. Lei, "Position sensorless control of switched reluctance motors based on angle adjustment using nonlinear inductance and flux model," *IEEE Transactions on Industrial Electronics*, Vol. 71, No. 12, 15 467–15 477, 2024.

[2] Wang, H., Y. Xue, J. Du, and H. Li, "Design and evaluation of modular stator hybrid-excitation switched reluctance motor for torque performance improvement," *IEEE Transactions on Industrial Electronics*, Vol. 71, No. 10, 12 814–12 823, 2024.

[3] Davarpanah, G., J. Faiz, H. Shirzad, and M. Lotfizadeh, "A modular hybrid excited switched reluctance motor with two groups of permanent magnets to enhance the performance of the motor," *IEEE Transactions on Energy Conversion*, Vol. 39, No. 3, 1686–1698, 2024.

[4] Tarımer, I. and R. Gurbuz, "Sizing of electrical motors for gearless and directly stimulating applications," *Elektronika Ir Elektrotechnika*, Vol. 84, No. 4, 21–26, 2008.

[5] Jabari, M. and A. Rad, "Optimization of speed control and reduction of torque ripple in switched reluctance motors using metaheuristic algorithms based PID and FOPID controllers at the edge," *Tsinghua Science and Technology*, Vol. 30, No. 4, 1526–1538, 2025.

[6] Cai, J., X. Dou, A. D. Cheok, W. Ding, Y. Yan, and X. Zhang, "Model predictive control strategies in switched reluctance motor drives — An overview," *IEEE Transactions on Power Electronics*, Vol. 40, No. 1, 1669–1685, 2025.

[7] Mohanraj, D., J. Gopalakrishnan, B. Chokkalingam, and J. O. Ojo, "An enhanced model predictive direct torque control of SRM drive based on a novel modified switching strategy for low torque ripple," *IEEE Journal of Emerging and Selected Topics in Power Electronics*, Vol. 12, No. 2, 2203–2213, 2024.

[8] Ali, T. F., D. A. Dominic, and P. Prabhakaran, "A systematic approach to digital control development for four-phase SRM drive using single current sensor for medium power applications," *IEEE Access*, Vol. 12, 34 074–34 088, 2024.

[9] Fang, G., J. Ye, D. Xiao, Z. Xia, and A. Emadi, "Computational-efficient model predictive torque control for switched reluctance machines with linear-model-based equivalent transformations," *IEEE Transactions on Industrial Electronics*, Vol. 69, No. 6, 5465–5477, 2022.

[10] Ren, P., J. Zhu, Y. Liu, Y. Zhao, and Z. Jing, "An improved model-predictive torque control of switched reluctance motor based on sector adaptive allocation technology," *IEEE Transactions on Power Electronics*, Vol. 39, No. 4, 4567–4577, 2024.

[11] Li, X. and P. Shamsi, "Model predictive current control of switched reluctance motors with inductance auto-calibration," *IEEE Transactions on Industrial Electronics*, Vol. 63, No. 6, 3934–3941, 2016.

[12] Han, G., L. Zhang, Y. Wang, S. Xu, and D. Yu, "Variable switching point model-free predictive current control strategy for SRM," *IEEE Transactions on Industrial Electronics*, Vol. 72, No. 5, 4470–4480, 2025.

[13] Nassereddine, K., M. Turzynski, H. Bielokha, and R. Strzelecki, "Simulation of energy management system using model predictive control in AC/DC microgrid," *Scientific Reports*, Vol. 15,

No. 1, 5388, 2025.

[14] Chen, Z., H. Jing, X. Wang, X. Wang, G. Fang, H. Zhao, and D. Xiao, "General-purpose high-speed position-sensorless control of switched reluctance motors using single-phase adaptive observer," *IEEE Transactions on Transportation Electrification*, Vol. 10, No. 3, 5241–5249, 2024.

[15] Sun, C., X. Sun, C. Garcia, J. Rodriguez, Z. Yang, and S. Han, "Model predictive current control of six-phase switched reluctance motor with enhanced robustness based on improved lehuy model," *IEEE Transactions on Transportation Electrification*, Vol. 11, No. 2, 6177–6187, 2025.

[16] Yang, W., S. Ding, and C. Ding, "Fast supertwisting sliding mode control with antipeaking extended state observer for path-tracking of unmanned agricultural vehicles," *IEEE Transactions on Industrial Electronics*, Vol. 71, No. 10, 12 973–12 982, 2024.

[17] Zhang, X., X. Yu, and G. Zhang, "Adaptive model predictive current control for PMSM drives based on bayesian inference," *IEEE Transactions on Power Electronics*, Vol. 40, No. 6, 8490–8502, 2025.

[18] Oliveri, A., M. Lodi, and M. Storace, "Nonlinear models of power inductors: A survey," *International Journal of Circuit Theory and Applications*, Vol. 50, No. 1, 2–34, 2022.

[19] Feng, L., X. Sun, G. Bramerdorfer, Z. Zhu, Y. Cai, K. Diao, and L. Chen, "A review on control techniques of switched reluctance motors for performance improvement," *Renewable and Sustainable Energy Reviews*, Vol. 199, 114454, 2024.